Journal of Asian Earth Sciences 117 (2016) 146–152

Contents lists available at ScienceDirect

Journal of Asian Earth Sciences

journal homepage: www.elsevier.com/locate/jseaes

Subtropical denudation rates of granitic regolith along a hill ridge in Longnan, SE China derived from cosmogenic nuclide depth-profiles

Li-Feng Cui [a,b], Cong-Qiang Liu [a,*], Sheng Xu [c], Zhi-Qi Zhao [a], Tao-Ze Liu [a], Wen-Jing Liu [d], Zhuo-Jun Zhang [a,b]

[a] State Key Laboratory of Environmental Geochemistry, Institute of Geochemistry, Chinese Academy of Sciences, Guiyang 550002, China
[b] University of the Chinese Academy of Sciences, Beijing 100029, China
[c] Scottish Universities Environmental Research Centre, Glasgow G75 0QF, UK
[d] Institute of Geology and Geophysics, Chinese Academy of Sciences, Beijing 100029, China

ARTICLE INFO

Article history:
Received 3 June 2015
Received in revised form 30 November 2015
Accepted 4 December 2015
Available online 8 December 2015

Keywords:
TCNs
^{10}Be
^{26}Al
Soil erosion
Chemical weathering
Geomorphic evolution

ABSTRACT

The denudation rates of granitic regolith are essential to our understanding of the geomorphic changes and landscape evolution of a region and for soil resource management. We present denudation rates derived from four regolith profiles along a granitic slope in Longnan, southeastern China, using depth profiles of in-situ produced cosmogenic ^{10}Be and ^{26}Al. The concentration ranges of ^{10}Be, ^{26}Al, and ^{26}Al/^{10}Be ratio were 2.98×10^4–1.72×10^5 atoms/g, 2.18×10^5–1.12×10^6 atoms/g, and 6.07–7.50, respectively. Analysis of the results shows that the surface-lowering rates are 19 ± 3, 41 ± 4, 47 ± 4, 22 ± 3 m/Ma for the four profiles from the foot of the hill to the top along the hillslope. The mean denudation rate for the four profiles is ~30 m/Ma. This rate is lower than that derived by other methods in nearby areas and also lower than the mean global denudation rate in basins deduced from ^{10}Be levels in river sediment; this suggests an unevenness of the erosion process on a basin scale. The denudation rate at the ridge is twice that estimated for the summit and the foothill, indicating that the hillslope has not reached its steady state. Thus, the slopes below the ridge may become smoother and the ridge sharper in the long-term landscape evolution. The difference in topography may account for the variance among the profiles. In addition, bioturbation may have contributed to the lower concentration in the surface layer at the foot of the hill, producing a higher denudation rate than the average for the basin. The concentration of insoluble element Zr in the soil surface layer and fresh bedrock suggests that chemical weathering accounts for about one third of the denudation rate.

1. Introduction

Earth's critical zone comprises the system of coupled chemical, biological, physical, and geological processes operating together to support life on the earth's surface. Both natural and human-related processes perturb this zone from vegetation canopy to bedrock (Brantley et al., 2007). As the main component of Earth's crust, granite is widely scattered on its surface. Regolith is the layer of physically, chemically, or biologically altered material that overlies non-weathered rock (Brantley and Lebedeva, 2011). The regolith that develops over the granite plays a key role in climate change, soil management, and landform evolution. The process of granite weathering is a CO_2-consuming reaction which effectively transfers the atmospheric or soil CO_2 to HCO_3^-. It has a long-term impact on the global carbon cycle and affects the global temperature to a great extent. The weathering rate of silicate may explain the missing carbon sink and help us understand the complex, nonlinear feedback processes acting among Earth's multiple systems, both internal factors (tectonic activities, mineral composition, chemical component, etc.) and external factors (temperature, precipitation, vegetation, etc.).

In-situ-generated terrestrial cosmogenic nuclides (TCNs) are produced in the upper few meters of the earth's surface by interactions between target atoms and secondary cosmic rays that reach the earth's surface via cascading processes (Lal, 1991). Generally, the production rate of cosmogenic nuclides attenuates rapidly with depth; therefore, measuring the concentration of TCNs can provide an indication of the rate at which material was removed from the sampling site (Granger, 2006; Lal, 1991). Since the advent of Accelerator Mass Spectrometry (AMS) in the 1980s, in-situ produced TCNs have been studied extensively to determinate the exposure

* Corresponding author.
E-mail address: liucongqiang@vip.skleg.cn (C.-Q. Liu).

http://dx.doi.org/10.1016/j.jseaes.2015.12.006
1367-9120/

age of alluvial fans (Riebe et al., 2000), terraces (Rodés et al., 2011), and moraines (Bierman et al., 1999), the buried age of sediments or a paleo-lake (Granger and Smith, 2000; Kong et al., 2009), and the denudation rate of soil, regolith, and rock (Rodés et al., 2011). Research on the earth's surface denudation rates based on the cosmogenic nuclide depth profile method in different climatic, tectonic, topographic, and lithological environments (Shiroya et al., 2010) is being carried out globally. However, only a few studies were conducted in China (Huang et al., 2013a, 2013b; Kong et al., 2007).

In this paper, in-situ cosmogenic ^{26}Al, ^{10}Be, and element Zr concentrations were measured to derive the denudation and chemical weathering rates of granite regolith at a hillslope in the subtropical Taojiang basin, a tributary of the Yangtze River. The term physical erosion is used to refer to the removal of mineral grains through the processes of bioturbation, rainsplash, freeze–thaw, landslides, etc. The term denudation is used when referring to the total mass loss by physical erosion and chemical weathering (Granger, 2006). We assume that the regolith reached steady-state, i.e., the regolith has been exposed for much longer than the effective exposure time; thus, the nuclide production and losses by denudation and radioactive decay have reached equilibrium (Matsushi et al., 2008; Shiroya et al., 2010).

2. Method and materials

2.1. Regional setting

The sampling site is located at the northern Nanling granite belt in Jiangxi Province, southeastern China (114°46′E, 24°58′N), at an altitude of 225 m above sea level (Fig. 1). The study area is in a subtropical zone with a humid monsoon climate. The local mean annual precipitation (MAP) is 1500 mm and the mean annual temperature (MAT) is 19 °C. A very thick (>10 m) layer of granitic regolith is widely distributed over this area, forming red soil in the upper layer. The landform is mostly hilly with a relief of ~300 m. The slope gradient of the hill is ~25° on both sides and ~18° along the ridge. The hillside has an east-facing slope and is mainly covered by coniferous forest. Tectonically, the research area lies southeast of the Eurasian continental plate and belongs to the Taojiang river basin. The profiles are located above the 470-km^2 Peitou pluton, the main lithology is moyite with a Rb–Sr isochron age of 178.15 ± 0.85 Ma, belonging to the Yanshanian tectonic period (Fan and Chen, 2000). Thus, few inherited cosmogenic nuclides ^{26}Al and ^{10}Be exist in the area. Moreover, because the granite has been exposed at the surface for a long period, it is reasonable to assume that the ^{26}Al and ^{10}Be in the regolith have reached a steady state. More geologic and pedological information can be found in Zhang et al. (2015). No volcanic activity has been recorded in this area since the Yanshanian epoch. The main tectonic activity in the Quaternary is slow uplift. Only 16 recorded earthquakes of magnitude 4.75–6 have occurred in the region since A.D. 1562 (Zhong, 2002).

2.2. Sampling and analysis

For the study site, we chose a granitic area with little human activity and collected a total of 15 samples from four depth profiles in one hillslope (Fig. 1c). Six samples were collected from profile S1, and three from each of the other three profiles (S2, S3, and S4).

The density of each sample was measured by packing it into a container of known volume. All the samples were first crushed and then sieved to keep the grain size fraction between 0.25 and 0.5 mm. The magnetic material was then eliminated in a magnetic separator. Next, the quartz was purified using the chemical etching method (Kohl and Nishiizumi, 1992). The Al concentrations were measured by ICP-OES to ensure the purity of the quartz. The purified quartz was spiked with Be carrier (~1000 μg) and dissolved with concentrated HF acid. This was followed by anion and cation exchange in a series of column chromatography procedures. The solution was neutralized by NH_4OH. The appearance of $Be(OH)_2$

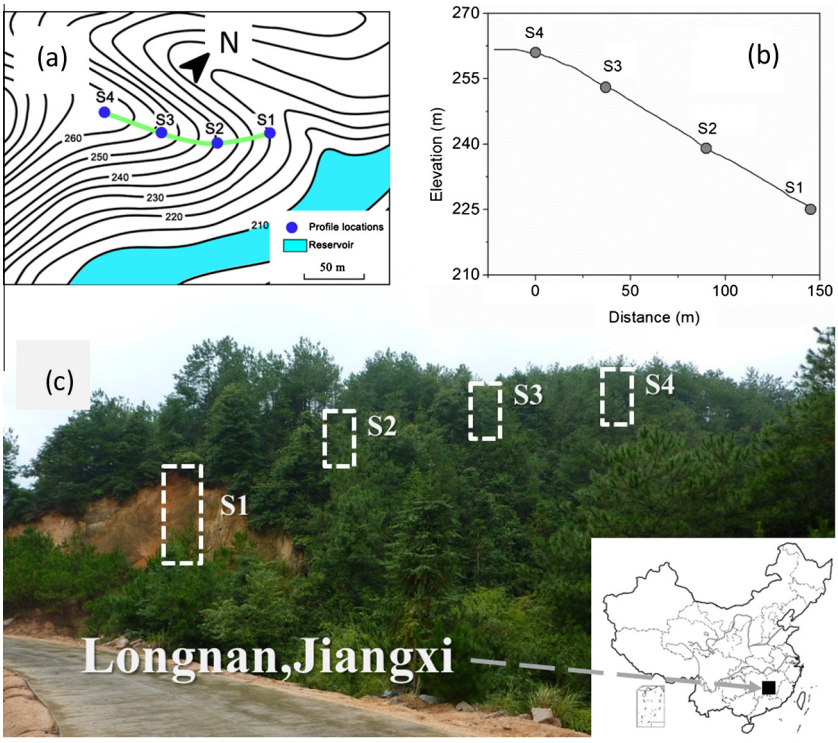

Fig. 1. (a) Contour map and profile distribution in Longnan. (b) Cross section of the 2D planar transects (S4–S1). (c) Location of study area and a view of the sampling site.

and $Al(OH)_3$ were oxidized to BeO and Al_2O_3. Then, Ag powder was mixed with Al_2O_3 and Nb powder added to BeO. Finally, the homogenized mixtures were pressed into a Cu holder for AMS measurements ($^{10}Be/^{9}Be$ and $^{26}Al/^{27}Al$) at the Scottish Universities Environmental Research Centre (Xu et al., 2010). The isotope ratios were normalized to the standard NIST_27900 for Be and Z92-0222 for Al.

2.3. Calculation method

2.3.1. Surface production rate

The in-situ cosmogenic nuclide surface production rates corresponding to the sampling site were calculated based on the sample location using the CRONUS-earth online calculator version 2.2 (Balco and Rovey, 2008). At the elevation (225 m) and latitude (24°58′N) of profile S1, the total surface production rates were 4.13 atoms/g a for ^{10}Be and 28.22 atoms/g a for ^{26}Al. The same production rates were derived for the other three profiles, being at similar elevation and latitude.

2.3.2. Shielding factors

The shielding of cosmic rays by mountains, slope surfaces, and vegetation can decrease the production rates of cosmogenic nuclides. With the thin coniferous forest covering the study sit, shielding by vegetation is not significant. The topographic shielding factor was calculated by mapping the angular elevation and azimuth (0–360°) of the points on the horizon around the profile using the online geometric shielding calculator in the CRONUS website (Balco et al., 2008; Dunne et al., 1999). The calculated shielding factor of the sampling site is 0.987.

2.3.3. The depth profile method

The analysis of a single cosmogenic nuclide is based on an ideal state, where the exposure time is much larger than the effective exposure time or where minimal erosion occurs during a very long period. Moreover, the analysis of the nuclide pair ^{10}Be–^{26}Al in one sample may reduce the precision of the date estimate. Therefore, we selected the depth profile method to determine both the denudation rate and the exposure time. The depth profile model is an effective method that uses the χ^2 best-fit distribution of the erosion rate and associated exposure age (Braucher et al., 2009; Siame et al., 2004).

Cosmogenic ^{10}Be and ^{26}Al are produced by three mechanisms – spallation, fast muons, and slow muon capture (Granger and Riebe, 2007). The production rate of in-situ cosmogenic nuclides decreases exponentially with depth; thus, the depth distribution of ^{10}Be and ^{26}Al can be expressed as

$$C(x,t) = \frac{P_{spal}}{\frac{\rho\cdot\varepsilon}{\Lambda_{spal}}+\lambda}\cdot e^{\frac{-\rho\cdot x}{\Lambda_{spal}}}\cdot\left(1-e^{-\left(\lambda+\frac{\rho\cdot\varepsilon}{\Lambda_{spal}}\right)\cdot t}\right)+\frac{P_{neg}}{\frac{\rho\cdot\varepsilon}{\Lambda_{neg}}+\lambda}\cdot e^{\frac{-\rho\cdot x}{\Lambda_{neg}}}\cdot\left(1-e^{-\left(\lambda+\frac{\rho\cdot\varepsilon}{\Lambda_{neg}}\right)\cdot t}\right)+\frac{P_{fast}}{\frac{\rho\cdot\varepsilon}{\Lambda_{fast}}+\lambda}\cdot e^{\frac{-\rho\cdot x}{\Lambda_{fast}}}\cdot\left(1-e^{-\left(\lambda+\frac{\rho\cdot\varepsilon}{\Lambda_{fast}}\right)\cdot t}\right) \quad (1)$$

where $C(x,t)$ is the cosmogenic nuclide concentration in the sample at depth x and exposure age t, P_{spal}, P_{stop}, and P_{fast} are the surface production rates of TCNs generated by spallation, slow muon capture, and fast muon reactions, respectively. ρ represents the density, ε is the denudation rate, and Λ is the effective attenuation length of the cosmic particles (Λ_{spal}: 160 g/cm^2, Λ_{neg}: 1257 g/cm^2, Λ_{fast}: 1988 g/cm^2). In this paper, the half-lives of ^{10}Be and ^{26}Al are 1.36 Ma and 0.7 Ma, respectively. Thus, the decay constant λ is 5.1×10^{-7}/a for ^{10}Be and 9.83×10^{-7}/a for ^{26}Al.

We assume that the profiles are in a steady-state condition; hence, the mass loss balances the generated regolith. Since the production of TCNs balances their decay and removal, Eq. (1) can be simplified to

$$C(x) = \frac{P_{spal}}{\frac{\rho\cdot\varepsilon}{\Lambda_{spal}}+\lambda}\cdot e^{\frac{-\rho\cdot x}{\Lambda_{spal}}}+\frac{P_{neg}}{\frac{\rho\cdot\varepsilon}{\Lambda_{neg}}+\lambda}\cdot e^{\frac{-\rho\cdot x}{\Lambda_{neg}}}+\frac{P_{fast}}{\frac{\rho\cdot\varepsilon}{\Lambda_{fast}}+\lambda}\cdot e^{\frac{-\rho\cdot x}{\Lambda_{fast}}} \quad (2)$$

2.3.4. χ^2 best fitting model

Using the samples located along the depth profile, the Chi-squared test is applied as an inversion method to adjust the parameters to find the theoretical value closest to the measured concentration (Braucher et al., 2009; Siame et al., 2004). This test was improved by Rodés et al. (2011). The two cosmogenic nuclides are joined in the model.

$$\chi^2 = \sum_{i=0}^{N}\left(\frac{C_i - C_{(x,\varepsilon,t)}}{\sigma_{i(\varepsilon,t)}}\right)^2+\sum_{j=0}^{M}\left(\frac{C_j - C_{(x,\varepsilon,t)}}{\sigma_{j(\varepsilon,t)}}\right)^2 \quad (3)$$

where i and j are the sample numbers for ^{10}Be and ^{26}Al, respectively, N, and M are the number of cosmogenic nuclide samples in the profile, x is the depth of sample i or j; ε is the denudation rate, t is the exposure time; C_i and C_j determine the concentration of sample i and j; σ is the analytical error at depth x, and $C(x,\varepsilon,t)$ represents the total theoretical cumulative concentration from Eq. (2). In this study, the sum of the Chi-square (χ^2) distribution is minimized using the software Wolfram Mathematica 9.

2.3.5. Chemical weathering

In pedogenetic processes, the soluble elements (K, Na, etc.) can be transported by soil water leaching, while the insoluble elements (Zr, Ti, etc.) in the top layer of the regolith will be enriched in the chemical weathering process. This enrichment can be used as an indicator of the weathering intensity (Kirchner et al., 2006; Riebe et al., 2001, 2003). We selected Zr as the target insoluble element in our study. The elemental compositions of the bedrock and the top layer were measured to separate the denudation (D) rate into physical erosion (E) and chemical weathering (W) according to Eq. (4)

$$W = D\left(1-\frac{[Zr]_{rock}}{[Zr]_{soil}}\right) \quad (4)$$

where $[Zr]_{rock}$ and $[Zr]_{soil}$ are the concentrations of Zr in the bedrock and soil, respectively, and the WIF is the weathering intensity factor:

$$WIF = \left(\frac{[Zr]_{soil}}{[Zr]_{rock}}-1\right) \quad (5)$$

3. Results and discussion

3.1. Analysis results

Table 1 shows the measured isotopic ratios $^{10}Be/^{9}Be$ and $^{26}Al/^{27}Al$, the concentrations of ^{10}Be and ^{26}Al in quartz, and the $^{10}Be/^{26}Al$ ratio. The concentrations of all the samples, except S1-1, decreased exponentially with depth at each profile. The lowest ratios of $^{10}Be/^{9}Be$ ($0.40\pm0.02\cdot10^{-13}$) and $^{26}Al/^{27}Al$ ($1.25\pm0.05\cdot10^{-13}$) are much higher than those of the blank sample ($2.6\pm0.6\cdot10^{-15}$ for $^{10}Be/^{9}Be$ and $2.9\pm1.2\cdot10^{-15}$ for $^{26}Al/^{27}Al$), indicating good quality control during the experimental process. The concentrations of ^{26}Al and ^{10}Be for fifteen samples of the four profiles are shown in Fig. 2. The data fall close to a straight line which is the theoretical ^{26}Al, ^{10}Be spallation production ratio.

Table 1
CRN data for samples collected from profiles S1–S4.

Sample ID	Depth (cm)	Quartz (g)	$^{10}Be/^{9}Be$ (10^{-13})	$^{26}Al/^{27}Al$ (10^{-13})	^{10}Be Conc. (10^{4} atoms/g)	^{26}Al Conc. (10^{4} atoms/g)	$^{26}Al/^{10}Be$	Density (g/cm^3)
S1-1	25 ± 5	23.8	2.60 ± 0.07	8.23 ± 0.22	16.05 ± 0.37	105.71 ± 7.79	6.59 ± 0.26	1.39
S1-2	55 ± 5	23.265	2.63 ± 0.06	8.31 ± 0.19	16.70 ± 0.34	112.28 ± 7.02	6.72 ± 0.20	1.53
S1-3	85 ± 5	23.781	2.20 ± 0.06	6.76 ± 0.18	13.42 ± 0.34	90.63 ± 6.74	6.75 ± 0.28	1.59
S1-4	135 ± 5	18.565	0.87 ± 0.03	2.54 ± 0.07	6.70 ± 0.23	47.31 ± 3.60	7.06 ± 0.35	1.63
S1-5	245 ± 5	21.657	0.72 ± 0.03	2.83 ± 0.10	4.73 ± 0.18	33.83 ± 3.48	7.16 ± 0.62	1.66
S1-6	385 ± 5	18.658	0.40 ± 0.02	1.25 ± 0.05	2.98 ± 0.13	21.77 ± 2.60	7.31 ± 0.87	1.67
S2-1	25 ± 5	19.546	1.20 ± 0.04	4.56 ± 0.14	8.90 ± 0.25	59.19 ± 5.01	6.65 ± 0.35	1.63
S2-2	55 ± 5	22.282	1.15 ± 0.03	4.10 ± 0.13	7.43 ± 0.20	52.59 ± 4.60	7.08 ± 0.42	1.75
S2-3	115 ± 5	21.358	0.78 ± 0.03	2.54 ± 0.09	5.23 ± 0.20	38.02 ± 3.66	7.26 ± 0.56	1.66
S3-1	25 ± 5	21.197	1.18 ± 0.04	2.80 ± 0.08	8.08 ± 0.24	53.70 ± 4.04	6.65 ± 0.29	1.58
S3-2	55 ± 5	20.868	0.87 ± 0.04	3.42 ± 0.12	5.98 ± 0.25	44.87 ± 4.21	7.50 ± 0.59	1.55
S3-3	115 ± 5	22.343	0.69 ± 0.03	2.06 ± 0.07	4.43 ± 0.18	31.41 ± 2.80	7.10 ± 0.48	1.60
S4-1	35 ± 2.5	20.968	2.45 ± 0.06	7.08 ± 0.20	17.19 ± 0.37	104.29 ± 7.86	6.07 ± 0.23	1.53
S4-2	55 ± 5	20.312	1.74 ± 0.05	4.67 ± 0.14	12.51 ± 0.33	77.84 ± 6.30	6.22 ± 0.28	1.54
S4-3	105 ± 5	22.822	1.49 ± 0.04	3.94 ± 0.11	9.51 ± 0.24	59.75 ± 4.66	6.29 ± 0.27	1.69
Blank	–	–	0.026 ± 0.006	0.029 ± 0.012	–	–	–	–

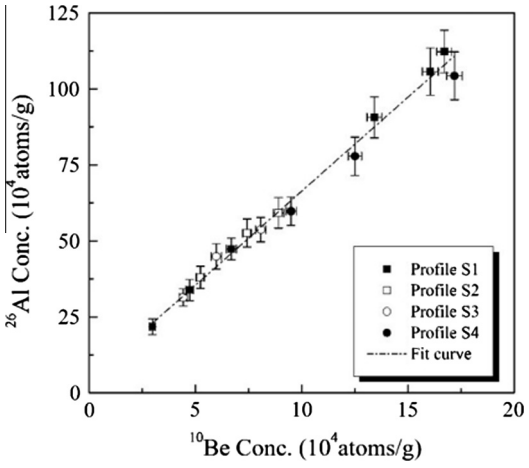

Fig. 2. Correlation of ^{10}Be and ^{26}Al concentrations.

3.2. Estimation of denudation rates

The distribution of cosmogenic ^{10}Be concentrations and their best-fit curves are shown in Fig. 3. Profile S1 in the foothills is the deepest one, with six samples; thus, profile S1 has a relatively well-constrained denudation rate and exposure age. The best fitting result for S1 shows a long-term mean denudation rate of 19 ± 3 m/Ma, close to the peak of profile S4 (22 ± 3 m/Ma). The denudation rate obtained from profiles S2 and S3 located on the ridge are about twice the rates of profiles S1 and S4 (41 ± 4 m/Ma for S2, 47 ± 4 m/Ma for S3). As shown in Fig. 6, the chemical index of alteration (CIA) has a sequence of S1 < S2 < S3 < S4. Ma et al. (2010) revealed that the residence time of regolith on a ridge is shorter than at the foothill and summit of a mountain. This is quite reasonable because the ridge (profiles S2 and S3) is the source of material for the hillslope on both sides. In this case, weathered material can flow from the peak down three slopes; thus, profile S4 should have the highest physical erosion rate. However, the results deviate from the theory, showing a relative lower denudation rate in profile S4 than in profiles S2 and S3. The CIA also indicates that profile S4 has the highest weathering intensity. Thus, the flat terrain on the summit may cause weak erosion. The denudation rate of profile S1 is comparable to S4. In contrast to this result, in the Susquehanna/Shale Hills Observatory, Pennsylvania, USA the regolith production rate at the valley floor was much lower than at the top of the ridge (Ma et al., 2010). Moreover, the process of soil creeping can remove surface debris from the upslope region in profile S4. It is likely that the profile has not yet reached its steady state. The distribution pattern of the χ^2 value of ^{10}Be in profile S1 (Fig. 4) indicates that the exposure age of profile S1 is ~0.3 Ma.

The concentrations of ^{10}Be and ^{26}Al in surface sample S1-1 are similar to those in S1-2. The denudation rate derived using the measurements from S1-1 is 34–41 m/Ma. However, sample S1-1 was treated as an outlier and was not included in the best-fit model. The sample may have been formed as a result of soil creeping or bioturbation (animal burrowing, tree throw, rooting, etc.) that led to the mixed soil layer. The effect of bioturbation was observed in some studies (Perg et al., 2001; Cockburn and Summerfield, 2004) where it was shown to generate a vertically mixed layer, leading to lower cosmogenic nuclide concentration on the surface than predicted by theoretical methods. Shiroya et al. (2010) demonstrated that the denudation rate of regolith may not be reliable based simply on comparison of surface samples.

The ^{26}Al–^{10}Be isotopes diagram (Bierman et al., 1999) is shown in Fig. 5. Most of the samples are scattered in the steady erosion "island" area with 1δ error, except the three samples from profile S4. Samples from the deep layer in profile S1 have larger errors because of the relative low concentrations, high measurement error, and higher muon production rates, which produce nuclides with higher $^{26}Al/^{10}Be$ ratios. The study site is in a large valley, 4 km wide and 300 m deep, near the surface of a main stream; hence, the low $^{26}Al/^{10}Be$ ratio of profile S4 suggests a short-term burial history that may have occurred during the evolution of the nearby higher geomorphic units. The burial history may be associated with both flooding and lateral erosion of the stream; the alluvial deposition may have covered some flat terrain during the short period when the flood events occurred.

3.3. Chemical weathering

The CIA of all the profiles and the bedrock was derived and is shown in Fig. 6. The CIA of profile S1 decreases with depth, except at the top soil layer. The mean concentration of Zr is 356 ppm in the S1 soil top layer (0–20 cm) and 240 ppm in the fresh bedrock. Substituting these values into Eq. (4) we obtain the chemical weathering rate which accounts for about 33% of the denudation rate, with WIF = 0.48. This is close to the result of Liu (2007) derived from river hydrochemistry and sediment analysis in a nearby region, where the chemical weathering rate was 37% of the total weathering rate.

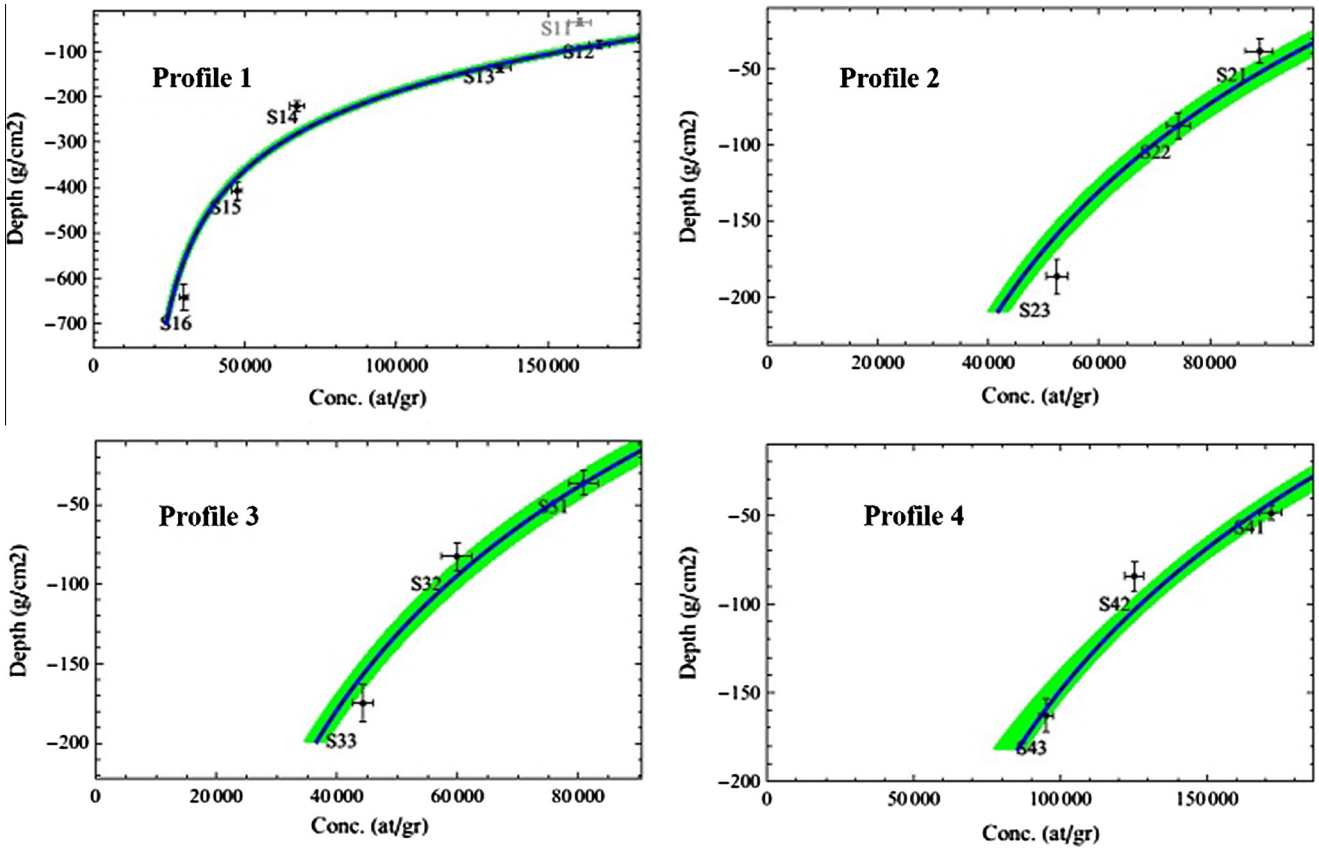

Fig. 3. ^{10}Be concentrations vs. depth (expressed as $x = -\rho \cdot z$; ρ is the density [g/cm^3], z is the current depth [cm]). Error bars show the uncertainties of concentration and depth. Black line is the best-fit model and gray area indicates the 1σ confidence zone.

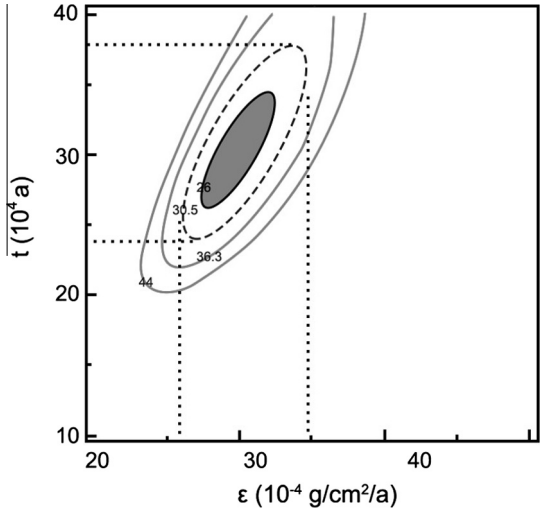

Fig. 4. The χ^2 value plot of ^{10}Be in profile S1. ε equals the product of denudation times density, t is the exposure time.

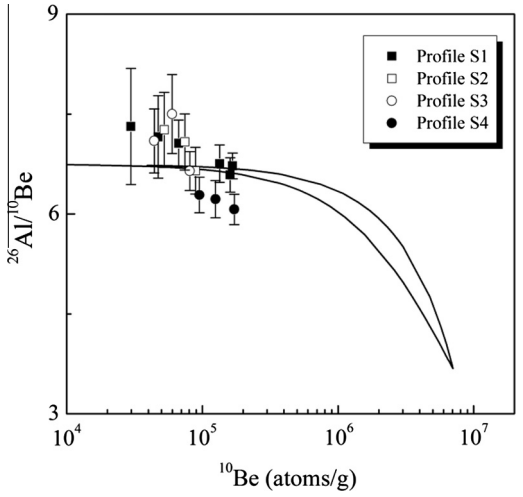

Fig. 5. ^{10}Be concentrations vs. ^{26}Al/^{10}Be ratio. The banana-like area is the steady erosion "island".

3.4. Comparison with other studies

Studies on erosion rates that use various methods were reported in China. These studies were conducted on different rock types, climate zones, and tectonic areas. To compare our study with other similar work, we selected the short-term erosion rates reported for similar climatic conditions with the same bedrock type. The weathering rate of granite in a small forested watershed in subtropical China, based on geochemical mass balance equations, is 66 ± 48 m/Ma (Huang et al., 2013b). The denudation rate in the southern Nanling Mountains, derived using the mass balance method, is 100 m/Ma, in which physical erosion accounts for 63% of the total erosion (Liu, 2007). According to the data compiled by Liu (2007), the mean erosion modulus of basins in China is 249.58 t/km^2/a; assuming a soil density of 1.6 g/m^3, the corresponding erosion rate is 156 m/Ma. The physical erosion rate of the Taojiang river for the period

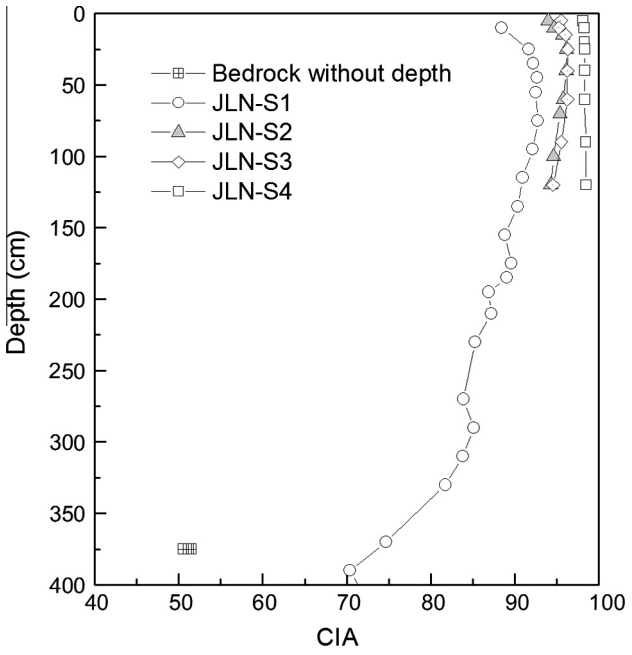

Fig. 6. The CIA distribution of profiles S1–S4 in Longnan. The bedrock depth is >15 m.

1959–2004, derived from sediment concentration levels, is about 113 m/Ma, (Gong et al., 2006). The denudation rates reported here are lower than the rates presented in the studies mentioned above because of the variance of time scales and hypotheses used in various research methods. Furthermore, in the Ganjiang watershed, a tributary of the Yangtze River, the denudation rates are 43 m/Ma based on the mass balance method and 20 m/Ma using the ^{10}Be method as a mean value over tens of thousands of years (Huang et al., 2013a).

Portenga and Bierman (2011) reviewed studies of Earth's surface erosion involving ^{10}Be. According to their statistics, the mean ^{10}Be erosion rate is 148 m/Ma in igneous basins and 12 m/Ma in outcrops. In temperate and tropical basins, the mean ^{10}Be erosion rates are 277 and 111 m/Ma, respectively (Portenga and Bierman, 2011). The denudation rates of granite regolith reported in our study are between their basin and outcrop values and much lower than the mean denudation rates of temperate and tropical basins. We added our results to the compiled global basin ^{10}Be dataset, and compared the relationships between denudation rate and the MAP and slope (Fig. 7). The MAP and slope are important internal and external factors affecting weathering and show statistically significant bivariate correlations with denudation rates. Compared with the temperate and tropical climatic zones, the denudation rate in our study is relatively low for the same slope and MAP. Similar work about granitic regolith was conducted in western Abukuma, Japan, yielding a regolith denudation rate of 49–74 m/Ma (Shiroya et al., 2010), slightly higher than our result.

Compared with basin scale denudation rates obtained from ^{10}Be concentrations in river sediment, the depth profile method is more accurate; however, it represents only a small local area and has limitation in terms of estimating large-scale denudation rates. Hence, for regional assessments, it is advantageous to combine these two methods to obtain more reliable and accurate denudation rates. Moreover, the U-series method was applied to estimate basin and regolith erosion rate in recent years (Dosseto et al., 2014; Ma et al., 2010; Suresh et al., 2013; Blisniuk et al., 2012; Chabaux et al., 2013). Using multiple methods to quantify surface erosion rates produces more reliable models of surface erosion and weathering processes and helps evaluate the feasibility of the various methods.

4. Conclusions

Based on the hypothesis that the regolith profiles at the study site have reached a steady state, the granite regolith on the Longnan slope has a mean denudation rate of 30 m/Ma, which is between the mean global values of igneous rocks and basins. Although the study area is controlled by a subtropical humid monsoon climate, the chemical weathering rate deduced from the insoluble element Zr in the surface soil and bedrock accounts for only about one third of the denudation rate (10 m/Ma). The ridge profile had a higher denudation rate than the other two profiles (at the foothill and the summit). The topography may be the main influencing factor for denudation rates at different sites. Compared with other studies on granite erosion rate, the denudation rates deduced from mass balance in a nearby river basin and from global ^{10}Be levels in river sediments in temperate and subtropical zones were higher than our result based on depth profiles, most likely because of the difference in the time scale and the bioturbation effect on the soil surface.

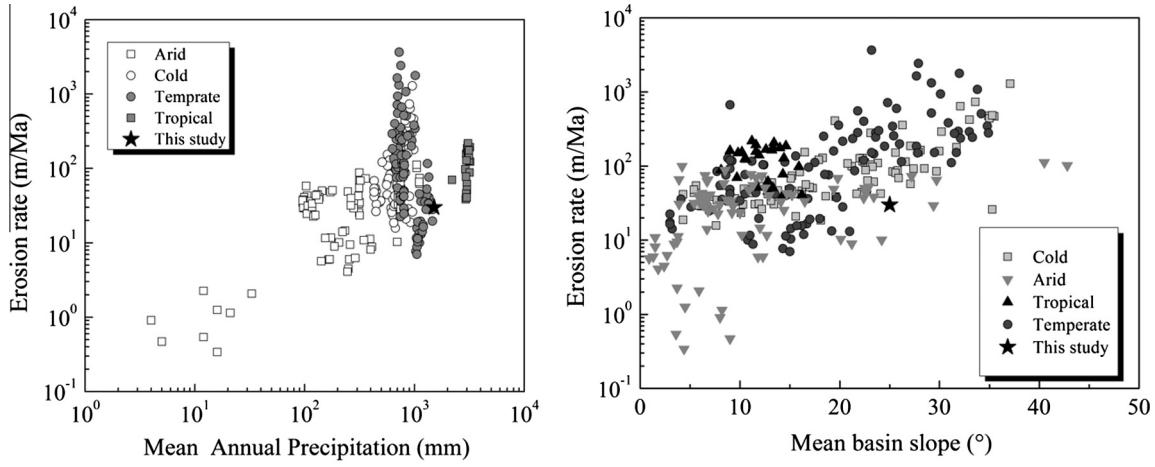

Fig. 7. Correlation between denudation rates and mean annual precipitation and basin slope in different climatic zones (data from Portenga and Bierman (2011) and references therein, and this study).

Conflict of interest

The authors declare that there are no conflicts of interest.

Acknowledgments

This study was funded by the National Natural Science Foundation of China (41130536, 41210004 and 2013CB956401) and the State Key Laboratory of Environmental Geochemistry, Institute of Geochemistry, Chinese Academy of Sciences (9014). We are grateful to M. Miguens-Rodriguez, A. Rodé, and K. Keefe their assistance in the experiments and data processing and to Fan Bailing and Liu Baojian for their assistance in sample collection.

References

Balco, G., Rovey, C.W., 2008. An isochron method for cosmogenic-nuclide dating of buried soils and sediments. Am. J. Sci. 308, 1083–1114.
Balco, G., Stone, J.O., Lifton, N.A., Dunai, T.J., 2008. A complete and easily accessible means of calculating surface exposure ages or erosion rates from ^{10}Be and ^{26}Al measurements. Quat. Geochronol. 3, 174–195.
Bierman, P.R., Marsella, K.A., Patterson, C., Davis, P.T., Caffee, M., 1999. Mid-Pleistocene cosmogenic minimum-age limits for pre-Wisconsinan glacial surfaces in southwestern Minnesota and southern Baffin Island: a multiple nuclide approach. Geomorphology 27, 25–39.
Blisniuk, K., Oskin, M., Fletcher, K., Rockwell, T., Sharp, W., 2012. Assessing the reliability of U-series and ^{10}Be dating techniques on alluvial fans in the Anza Borrego Desert, California. Quat. Geochronol. 13, 26–41.
Brantley, S.L., Lebedeva, M., 2011. Learning to read the chemistry of regolith to understand the critical zone. Annu. Rev. Earth Planet. Sci. 39, 387–416.
Brantley, S.L., Goldhaber, M.B., Ragnarsdottir, K.V., 2007. Crossing disciplines and scales to understand the Critical Zone. Elements 3, 307–314.
Braucher, R., Del Castillo, P., Sinme, L., Hidy, A.J., Bourlès, D., 2009. Determination of both exposure time and denudation rate from an in situ-produced ^{10}Be depth profile: a mathematical proof of uniqueness. Model sensitivity and applications to natural cases. Quat. Geochronol. 4, 56–67.
Chabaux, F., Blaes, E., Stille, P., di Chiara Roupert, R., Pelt, E., Desseto, A., Ma, L., Buss, H.L., Brantley, S.L., 2013. Regolith formation rate from U-series nuclides: implications from the study of a spheroidal weathering profile in the Rio Icacos watershed (Puerto Rico). Geochim. Cosmochim. Acta 100, 73–95.
Cockburn, H.A.P., Summerfield, M.A., 2004. Geomorphological applications of cosmogenic isotope analysis. Prog. Phys. Geogr. 28, 1–42.
Dosseto, A., Buss, H.L., Chabaux, F., 2014. Age and weathering rate of sediments in small catchments: the role of hillslope erosion. Geochim. Cosmochim. Acta 132, 238–258.
Dunne, J., Elmore, D., Muzikar, P., 1999. Scaling factors for the rates of production of cosmogenic nuclides for geometric shielding and attenuation at depth on sloped surfaces. Geomorphology 27, 3–11.
Fan, C., Chen, P., 2000. Geochemical characteristics and tectonic implication of Beitou A-type granitic intrusive in South Jiangxi Province. Geochimica 29, 358–366 (in Chinese with English abstract).
Gong, X., Li, K., Wang, S., Liang, X., 2006. Study of the sand changing law in granjiang basin and mankind activity. Jiangxi Hydraul. Sci. Technol. 32, 24–27 (in Chinese with English abstract).
Granger, D.E., 2006. A review of burial dating methods using ^{26}Al and ^{10}Be. Geol. Soc. Am. Spec. Pap. 415, 1–16.
Granger, D.E., Riebe, C.S., 2007. Cosmogenic nuclides in weathering and erosion. In: Turekian, K.K., Holland, H.D. (Eds.), Treatise on Geochemistry, Oxford, pp. 1–43.
Granger, D.E., Smith, L.A., 2000. Dating buried sediments using radioactive decay and muogenic production of ^{26}Al and ^{10}Be. Nucl. Instrum. Methods B 172, 822–826.
Huang, L., Zhang, G., Yang, J., 2013a. Weathering and soil formation rates based on geochemical mass balances in a small forested watershed under acid precipitation in subtropical China. CATENA 105, 11–20.
Huang, X., Zheng, H., Chappell, J., Wang, P., 2013b. Characteristics of cosmogenic nuclide ^{10}Be in the Yangtze riverine sediments and estimations of erosion rate. Quat. Sci. 33, 671–683 (in Chinese with English abstract).
Kirchner, J., Riebe, C.S., Ferrier, K., Finkel, R., 2006. Cosmogenic nuclide methods for measuring long-term rates of physical erosion and chemical weathering. J. Geochem. Explor. 88, 296–299.
Kohl, C.P., Nishiizumi, K., 1992. Chemical isolation of quartz for measurement of in-situ-produced cosmogenic nuclides. Geochim. Cosmochim. Acta 56, 3583–3587.
Kong, P., Na, C., Fink, D., Huang, F.X., Ding, L., 2007. Cosmogenic ^{10}Be inferred lake-level changes in Sumxi Co basin, Western Tibet. J. Asian Earth Sci. 29, 698–703.
Kong, P., Granger, D.E., Wu, F., Caffee, M.W., Wang, Y.J., Zhao, X.T., Zheng, Y., 2009. Cosmogenic nuclide burial ages and provenance of the Xigeda paleo-lake: implications for evolution of the Middle Yangtze River. Earth Planet. Sci. Lett. 278, 131–141.
Lal, D., 1991. Cosmic ray labeling of erosion surfaces: in situ nuclide production rates and erosion models. Earth Planet. Sci. Lett. 104, 424–439.
Liu, J., 2007. A Study on Denudation Rate for Southern Slope of Nanling Mountains, China. South China Normal University, pp. 1–62 (in Chinese with English abstract).
Ma, L., Chabaux, F., Pelt, E., Blaes, E., Jin, L., Brantley, S., 2010. Regolith production rates calculated with uranium-series isotopes at Susquehanna/Shale Hills Critical Zone Observatory. Earth Planet. Sci. Lett. 297, 211–225.
Matsushi, Y., Matsuzaki, H., Matsukura, Y., 2008. Potential of in situ-produced cosmogenic nuclides for quantifying strength reduction of bedrock in soil-mantled hillslopes. Quat. Geochronol. 3, 262–267.
Perg, L.A., Anderson, R.S., Finkel, R.C., 2001. Use of a new ^{10}Be and ^{26}Al inventory method to date marine terraces, Santa Cruz, California, USA. Geology 29, 879–882.
Portenga, E.W., Bierman, P.R., 2011. Understanding Earth's eroding surface with ^{10}Be. GSA Today 21, 4–10.
Riebe, C.S., Kirchner, J.W., Granger, D.E., Finkel, R.C., 2000. Erosional equilibrium and disequilibrium in the Sierra Nevada, inferred from cosmogenic ^{26}Al and ^{10}Be in alluvial sediment. Geology 28, 803–806.
Riebe, C.S., Kirchner, J.W., Granger, D.E., Finkel, R.C., 2001. Strong tectonic and weak climatic control of long-term chemical weathering rates. Geology 29, 511–514.
Riebe, C.S., Kirchner, J.W., Finkel, R.C., 2003. Long-term rates of chemical weathering and physical erosion from cosmogenic nuclides and geochemical mass balance. Geochim. Cosmochim. Acta 67, 4411–4427.
Rodés, Á., Pallàs, R., Braucher, R., Moreno, X., Masana, E., Bourlés, D.L., 2011. Effect of density uncertainties in cosmogenic ^{10}Be depth-profiles: dating a cemented Pleistocene alluvial fan (Carboneras Fault, SE Iberia). Quat. Geochronol. 6, 186–194.
Shiroya, K., Yokoyama, Y., Matsuzaki, H., 2010. Quantitative determination of long-term erosion rates of weathered granitic soil surfaces in western Abukuma, Japan using cosmogenic ^{10}Be and ^{26}Al depth profile. Geochem. J. 44, 23–27.
Siame, L., Bellier, O., Braucher, R., Sébrier, M., Cushing, M., Bourlès, D., Hamelin, B., Baroux, E., de Voogd, B., Raisbeck, G., 2004. Local erosion rates versus active tectonics: cosmic ray exposure modelling in Provence (south-east France). Earth Planet. Sci. Lett. 220, 345–364.
Suresh, P.O., Dosseto, A., Hesse, P.P., Handley, H.K., 2013. Soil formation rates determined from Uranium-series isotope disequilibria in soil profiles from the southeastern Australian highlands. Earth Planet. Sci. Lett. 379, 26–37.
Xu, S., Dougans, A.B., Freeman, S., Schnabel, C., Wilcken, K., 2010. Improved ^{10}Be and ^{26}Al AMS with a 5 MV spectrometer. Nucl. Instrum. Methods B 268, 736–738.
Zhang, Z., Liu, C., Zhao, Z., Cui, L., Liu, W., Liu, T., Liu, B., Fan, B., 2015. Behavior of redox-sensitive elements during weathering of granite in subtropical area using X-ray absorption fine structure spectroscopy. J. Asian Earth Sci. 105, 418–429.
Zhong, J., 2002. Research on the relationship between the geotectonic features and the distribution of earthquake in the south of Jiangxi South China. J. Seismol. 22, 45–53 (in Chinese with English abstract).